PNAS RESEARCH ARTICLE | CELL BIOLOGY OPEN ACCESS

A quantitative and spatial analysis of cell cycle regulators during the fission yeast cycle

Scott Curran[a], Gautam Dey[b,1], Paul Rees[c,d], and Paul Nurse[a,e,2]

Edited by Brenda Andrews, University of Toronto, Toronto, ON, Canada; received April 8, 2022; accepted July 27, 2022

We have carried out a systems-level analysis of the spatial and temporal dynamics of cell cycle regulators in the fission yeast *Schizosaccharomyces pombe*. In a comprehensive single-cell analysis, we have precisely quantified the levels of 38 proteins previously identified as regulators of the G2 to mitosis transition and of 7 proteins acting at the G1- to S-phase transition. Only 2 of the 38 mitotic regulators exhibit changes in concentration at the whole-cell level: the mitotic B-type cyclin Cdc13, which accumulates continually throughout the cell cycle, and the regulatory phosphatase Cdc25, which exhibits a complex cell cycle pattern. Both proteins show similar patterns of change within the nucleus as in the whole cell but at higher concentrations. In addition, the concentrations of the major fission yeast cyclin-dependent kinase (CDK) Cdc2, the CDK regulator Suc1, and the inhibitory kinase Wee1 also increase in the nucleus, peaking at mitotic onset, but are constant in the whole cell. The significant increase in concentration with size for Cdc13 supports the view that mitotic B-type cyclin accumulation could act as a cell size sensor. We propose a two-step process for the control of mitosis. First, Cdc13 accumulates in a size-dependent manner, which drives increasing CDK activity. Second, from mid-G2, the increasing nuclear accumulation of Cdc25 and the counteracting Wee1 introduce a bistability switch that results in a rapid rise of CDK activity at the end of G2 and thus, brings about an orderly progression into mitosis.

genetics | yeast | cell cycle

Significance

Across eukaryotes, the increasing level of cyclin-dependent kinase (CDK) activity drives progression through the cell cycle. As most cells divide at specific sizes, information responding to the size of the cell must feed into the regulation of CDK activity. In this study, we use fission yeast to precisely measure how proteins that have been previously identified in genome-wide screens as cell cycle regulators change in their levels with cell cycle progression. We identify the mitotic B-type cyclin Cdc13 and the mitotic inhibitory phosphatase Cdc25 as the only two proteins that change in both whole-cell and nuclear concentration through the cell cycle, making them potential candidates for universal cell size sensors at the onset of mitosis and cell division.

Steady-state growing eukaryotic cells generally coordinate their cell cycles with cell growth by ensuring that mitosis and the associated cell division take place when a particular cell size is attained (1–3). The mechanisms that bring about mitotic onset are known to be accurate because cell size at mitosis exhibits little variation, and are efficiently homeostatic because perturbation from a mean population size at mitosis is corrected within one to two subsequent cycles (4, 5). These control mechanisms are also integrated with cell ploidy as cells roughly double their size at mitosis with each doubling of DNA content (6–9). Given the conservation of genes involved in cell cycle control from yeasts to mammalian cells (10) and that coordination of mitosis and cell division with cell size is observed across eukaryotes, the molecular mechanisms involved are likely to share commonalities. A number of models for monitoring cell size have been proposed (11–17), with one of the most straightforward being for changes in the concentration of a mitotic regulatory component to accompany cell size increase until a threshold level is reached that allows mitosis to proceed (18). This may be achieved either by an increase in the concentration of a mitotic activator or by a decrease in the concentration of an inhibitor (11, 12). Such cell size–sensing mechanisms could be integrated with the monitoring of ploidy by interactions such as titration of activators or inhibitors onto the DNA or chromatin (19). These sensing mechanisms must also be coupled to the activation of the cyclin-dependent kinase (CDK), which brings about mitosis followed by cell division in all eukaryotes (20). The dynamics of CDK activation must be such that there is a sharp and irreversible entry into mitosis, which could be influenced by the molecular mechanisms sensing cell size. In this paper, we investigate these mechanisms by measuring the levels of mitotic regulators during the cell cycle both in the whole cell and in the nucleus where critical mitotic events occur. These studies of the levels of mitotic regulators in single cells are aimed at informing our understanding of how cells sense their size and regulate the dynamics of CDK activation during the cell cycle and at the onset of mitosis.

The fission yeast *Schizosaccharomyces pombe* is an ideal model organism for investigating the coordination of mitosis with cell size as 99% of genes (5,059 genes) have previously been deleted (21) and systematically screened for cell cycle phenotypes (22). This screen uncovered a total of 513 cell cycle genes. Two further screens of this collection revealed genes that specifically regulate mitotic signaling. One exploited heterozygous deletions of diploid cells where gene expression levels are reduced to half of normal to

Author affiliations: [a]Cell Cycle Laboratory, The Francis Crick Institute, London, NW1 1AT, United Kingdom; [b]Medical Research Council Laboratory for Molecular Cell Biology, London, WC1E 6BT, United Kingdom; [c]College of Engineering, Swansea University, Swansea, SA1 8EN, United Kingdom; [d]Imaging Platform Broad Institute of Harvard and Massachusetts Institute of Technology, Cambridge, MA 02142; and [e]Laboratory of Yeast Genetics and Cell Biology, Rockefeller University, New York, NY 10065

Author contributions: S.C. and P.N. designed research; S.C. performed research; S.C., G.D., P.R., and P.N. analyzed data; and S.C. and P.N. wrote the paper.

The authors declare no competing interest.

This article is a PNAS Direct Submission.

[1]Present address: Cell Biology and Biophysics, European Molecular Biology Laboratory, 69117 Heidelberg, Germany.

[2]To whom correspondence may be addressed. Email: paul.nurse@crick.ac.uk.

This article contains supporting information online at http://www.pnas.org/lookup/suppl/doi:10.1073/pnas.2206172119/-/DCSupplemental.

Published August 29, 2022.

identify haploinsufficient genes, whereby cells are either advanced or delayed into mitosis at a smaller or larger size, respectively. This screen identified 17 genes (23). A second screen covering 82% of viable haploid deletions (totaling 2,969 genes) identified 18 genes that were advanced into the G2 to mitosis transition at a smaller size (24). These genes encode proteins that are rate limiting for entry into mitosis, three of which overlapped with the haploinsufficiency study. Together, these two screens identified 32 genes encoding potential mitotic regulatory molecules that also serve as candidates for cell size sensing. This gene set includes those encoding proteins at the core of the CDK cell cycle control network, such as the main CDK in fission yeast Cdc2, the G2/mitosis B-type cyclin Cdc13, the activating phosphatase Cdc25, and the inhibitory protein kinase Wee1 (25–28).

A further reason why fission yeast lends itself well to the study of cell cycle regulation is because their simple rod-shaped geometry and growth by tip extension allow for cell cycle position to be determined by cell length (29). Changes in the levels of molecules during the cell cycle can, therefore, be determined in asynchronous, steady-state growing cultures by measuring the levels of endogenously tagged fluorescent proteins in single cells. Such a method avoids any perturbations induced by synchronizing procedures, which can disturb measurements of protein levels. Using two independent single-cell approaches, we have accurately measured the precise concentrations and absolute levels of these potential mitotic regulators in the whole cell and nucleus for up to hundreds of thousands of cells at single-cell resolution throughout the cell cycle. This study has identified the subset of mitotic regulators that exhibit changes in their whole-cell or nuclear concentration, making them prime candidates for cell size or ploidy sensors whose readout tunes the dynamics of CDK activity. These proteins are conserved across many eukaryotes and therefore, may be of universal relevance.

Results

Progression through the fission yeast cell cycle is concomitant with growth of the cell by tip extension, allowing for cell length to be used as an indicator of cell cycle position (Fig. 1*A*). Fission yeast cells have a very short G1, which occurs after mitotic exit. Binucleate and septated cells contain two 1C nuclei, which undergo S-phase as cell division takes place. Thus, taking account of cell length and whether cells are mononucleate, binucleate, or binucleate and septated allows for the specification of the fission yeast cell cycle. To assess the changes in the levels of mitotic regulatory molecules during the cell cycle, we endogenously tagged 30 proteins encoded by genes identified in the previously described haploinsufficiency and rate-limiting screens with single-color fluorescent labels in individual wild-type fission yeast strains. (The 30 excludes *nsp1* and *nup186* from the original 32 because these 2 showed no measurable fluorescence when tagged.) We also tagged eight more genes that could be involved in mitotic control, including *cdr2*, *plo1*, and *pyp3*, and for comparative purposes, nine further genes acting at the G1- to S-phase transition (*cdc10*, *cdc18*, *cdc20*, *cig1*, *cig2*, *mik1*, *puc1*, *rum1*, and *srw1*). All genes were tagged with mNeonGreen, chosen for its fast maturation time and bright signal (30), other than *wee1* (N-terminal GFP) (31), *cdc13* (internal superfolder GFP) (32), and *pka1* (C-terminal GFP) (*SI Appendix*, Table S1 has the full list of tagged proteins). To check that tagging of these genes did not have a major effect on cell size at mitotic onset, the length at septation was measured for all of the strains (*SI Appendix*, Fig. S1). There were negligible effects for the majority, the exceptions being the tagging of *wee1* and *pyp1*, which induced elongation, and *cdr1* and *ppa2*, which induced shortening (*SI Appendix*, Fig. S1 *A* and *C*). This suggests there is some loss of function for Cdr1, Ppa2, and Pyp1 and perhaps, stabilization of Wee1 due to the tagging.

Each strain was individually imaged using imaging flow cytometry (Amnis Imagestream X) from exponentially growing asynchronous cell cultures. This allowed us to image >100,000 cells per strain in each experiment, giving high cell cycle coverage. Bright-field segmentation masks were overlaid onto fluorescence images (Fig. 1*B*) to allow for cell intensity measurements (Fig. 1 *C*–*H*). For each strain, we plotted the mean fluorescence intensity relative to its own minimum against cell length to give an indication of the fold change of the protein level across the cell cycle (Fig. 1 *F*–*H*). We show the data for three example strains (Fig. 1 *C*–*E*): one that is constant in whole-cell concentration through the cell cycle, Cdc2-mNG (Fig. 1*C*), and two that show changes, Cdc13-sfGFP (Fig. 1*D*) and Cdc25-mNG (Fig. 1*E*). As expected for a mitotic B-type cyclin, Cdc13 accumulates as cell size increases and falls at the end of the cell cycle. Cdc25 showed an unexpected pattern of change by oscillating in level through the cell cycle. Its concentration fell with cell size increase in the first third of the cycle before reaccumulation from mid-G2 to a peak at mitotic onset.

The data for genes encoding mitotic regulatory proteins are shown in Fig. 1*F*, for proteins acting at the G1- to S-phase transition are shown in Fig. 1*G*, and for other potential regulators of mitotic control are shown in Fig. 1*H*. The data for G1- to S-phase transition proteins excluded data for Cig1, whose G2 levels were too low to meaningfully plot, and Rum1, which was not visible under physiological growth conditions. What is striking about our results is that the vast majority of potentially mitotic regulatory molecules showed almost no change in concentration as cell size increased during the cell cycle. The changes were often less than 1.1× and at most, 1.3×, with no evidence for a consistent increase in concentration as cells increased in size. The two exceptions of the 38 mitotic control cell cycle proteins assayed were Cdc13 and Cdc25 (Fig. 1 *D*–*F*), which change as cell size increases. The concentrations of both Cdc13 and Cdc25 peak at mitosis, and so, these proteins are candidates for being cell size–sensing regulatory molecules at the G2 to mitosis transition as has been suggested previously (11, 17, 33).

The situation with respect to the proteins acting at the G1- to S-phase transition is different. Of the seven proteins assayed (excluding Cig1 and Rum1), Cdc18 and Mik1 showed a significant change in concentration of up to sixfold, Cig2 and Srw1 increased almost twofold, and Puc1 less so (Fig. 1*G*; full scaling is shown in *SI Appendix*, Fig. S1*D*). Consistent with their expression being induced by the transcriptional activity of Cdc10 at the G1–S transition, Cig2, Cdc18, and Mik1 all peak at G1/S and then, fall in level as the cells proceed through G2. In the case of Cdc18 and Mik1, their concentrations peak as cells proceed through mitosis, while Cig2, Puc1, and Srw1 all peak after mitosis. We conclude that protein concentration changes appear to be more of a feature of the G1- to S-phase transition than is the case for the G2 to mitosis transition. The reductions in concentrations of these proteins observed as cells increase in size through G2 to mitosis could in principle indicate that they have a role in coordinating cell size increase with mitotic onset, but there is no evidence from our previous screens that the loss of any of these seven genes influences cell size at mitosis (23, 24).

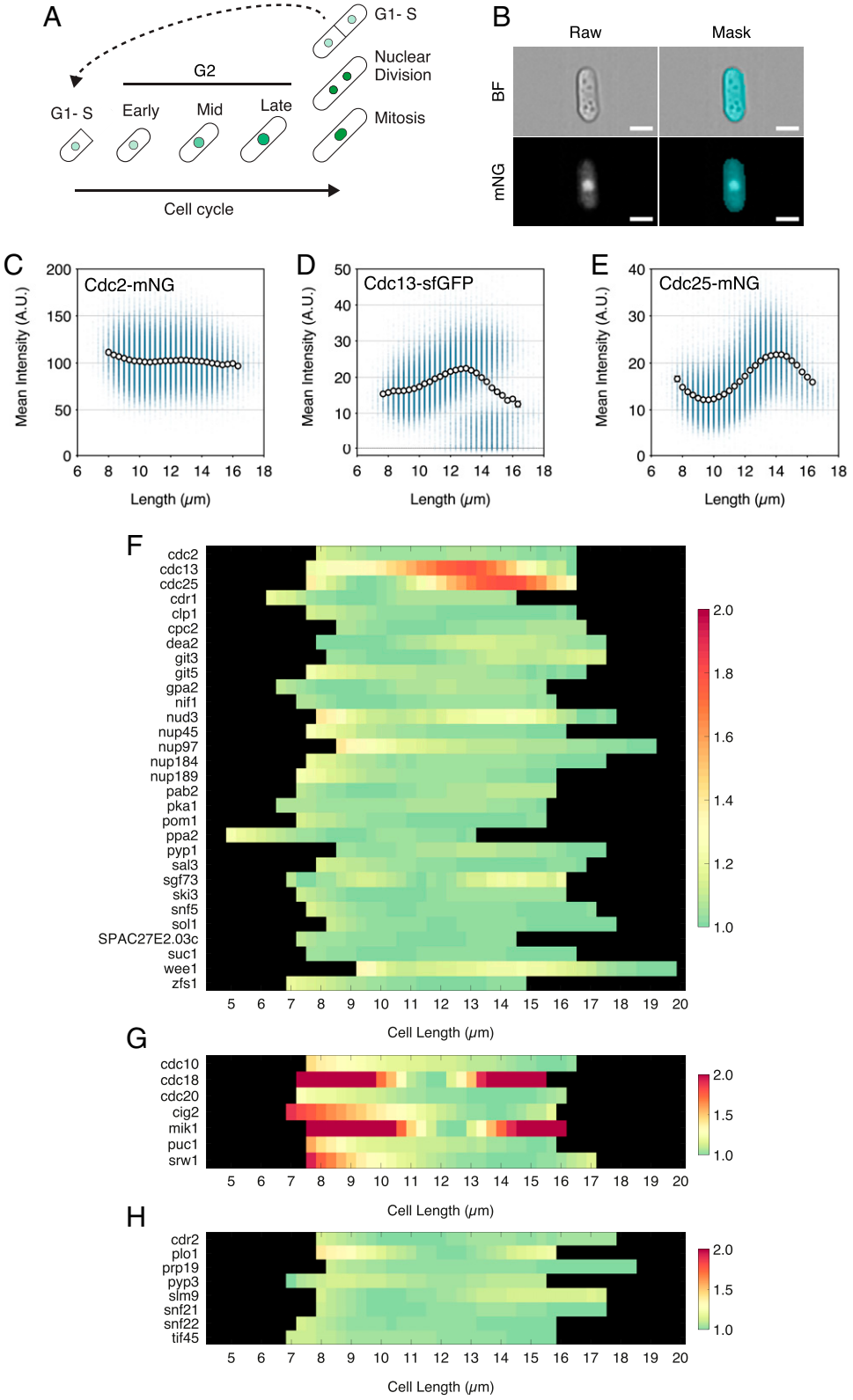

Fig. 1. Only Cdc13 and Cdc25 increase in whole-cell concentration to a peak at mitotic entry. (*A*) Schematic of the fission yeast cell cycle. Cells increase in length with progression through G2. Green indicates a representative protein that increases in nuclear concentration with cell cycle progression and increasing cell length that decreases in nuclear concentration after nuclear division. Cell growth slows as cells enter mitosis and undergo nuclear division. G1 and S phase occur in binucleates as cells septate. For YeaZ cell segmentation, binucleate cells are split at the point of septation, so cells in G1–S are the shortest cells in the plots for Figs. 2–4. (*B*) Representative images of a mononucleate Cdc2-mNG cell imaged by imaging flow cytometry. (*Upper Left*) Bright field. (*Lower Left*) mNG. (*Upper Right*) Segmentation mask of a BF image. (*Lower Left*) Overlay of the mask onto the fluorescent image. (Scale bars: 5 μm.) (*C*–*E*) Plots of imaging flow cytometry data for Cdc2-mNG (*C*), Cdc13-sfGFP (*D*), and Cdc25-mNG (*E*) populations showing mean whole-cell fluorescence intensity against cell length. Blue dots represent values for individual cells. Black circles indicate means. Error bars = 95% CIs. Length bins = 0.33 μm, with >500 cells/bin. AU, arbitrary units. (*C*) *n* = 185,376 cells. (*D*) *n* = 173,016 cells. (*E*) *n* = 180,023 cells. (*F*) Heat map showing the mean cellular fluorescence intensity for asynchronous populations of strains fluorescently tagged for mitotic regulators. Mean intensity for each 0.33-μm-length bin is normalized to each strain's minimum and plotted against cell length (>500 cells/bin). All strains are endogenously tagged with mNG, except for Cdc13 (internal sfGFP), Wee1 (N-terminal GFP), and Pka1 (C-terminal GFP). (*G* and *H*) The same as *F* except (*G*) for G1- to S-phase transition genes and (*H*) for other genes of interest involved in mitotic control.

We next turned from imaging flow cytometry to wide-field microscopy, which allowed us to investigate changes in cell cycle protein levels as well as spatial distributions. Utilizing a camera with a large field of view and using accurate cell segmentation with the neural network segmentation software YeaZ (34), we could image thousands of cells at high spatial resolution. Septating G1 cells were analyzed separately even if still physically connected (Fig. 1*A*).

The proteins analyzed in this study cover a broad range of regulatory and biological pathways (23, 24). Visual inspection revealed a range of localization patterns, including the cytoplasm, nucleus, spindle, spindle pole body (SPB), cell tips, and septum. (Images and descriptions of all strains used in this study are available in the extended supplementary information at https://figshare.com/articles/dataset/ExtendedSI_PNAS_Curran_2022_pdf/20362389/2 (35). Of the 47 proteins examined, 36 showed a nuclear localization, 29 of which accumulated at a higher level in the nucleus compared with the cytoplasm and 7 of which showed accumulation at the SPB (Cdc2, Cdc13, Clp1, Suc1, Wee, Cig1, Cig2, and Cdr2). For each strain, we plotted the whole-cell mean intensity vs. length and absolute intensity vs. length. Focusing first on the mitotic regulatory proteins analyzed in Fig. 1*F*, we confirmed that only Cdc13 (Fig. 2*F*) and Cdc25 (Fig. 2*J*) changed their whole-cell concentrations to peak at mitotic entry, with patterns of increase across the cell cycle similar to those observed from imaging flow cytometry (Fig. 1*F*).

Next, we turned our attention to changes in the localized concentration of proteins during the cell cycle. Due to the localization of proteins being specific to each strain, we calculated a mean of a top percentage of pixels in order to estimate local changes in concentration. Particular attention was paid to levels in the nucleus as a mitotic regulatory protein at this location could be indicative of an interaction with DNA and thus, ploidy sensing. The nuclear volume in fission yeast increases as cells proceed through the cell cycle as a fixed proportion of cell size (9, 36–38). In a two-dimensional image, the nucleus occupies ∼15% of the total cell area, so for strains that appeared to be nuclear localized, we approximated the changes in nuclear level from single-color imaging by determining the mean of the top 15% of pixels (nuclei could not be segmented from single-color imaging for proteins that leave the nucleus at mitosis, such as Cdc2 and Cdc13). This analysis allowed for a rapid and indicative screen of the "nuclear" localization behavior of the cell cycle proteins. Of the 29 proteins that preferentially localized to the nucleus, 12 showed concentration changes through the cell cycle (Cdc2, Cdc10, Cdc13, Cdc18, Cdc25, Cig1, Cig2, Clp1, Mik1, Srw1, Suc1, and Wee1). Five of the 12 peaked in concentration at the G2 to mitosis transition: Cdc2 (Fig. 2*D*), Cdc13 (Fig. 2*H*), Cdc25 (Fig. 2*L*), Suc1 (Fig. 2*P*), and Wee1 (Fig. 2*T*). Cdc13 (Fig. 2 *F* and *H*) and Cdc25 (Fig. 2 *J* and *L*) both showed similar patterns of increase in the "nucleus" as in the whole cell. Cdc2 (Fig. 2 *B* and *D*), Suc1 (Fig. 2 *N* and *P*), and Wee1 (Fig. 2 *R* and *T*) all exhibited nuclear concentration increases with increasing cell size, while their whole-cell concentrations remained constant. Clp1 showed a dynamic change in localization from the nucleolus and SPB to the spindle (Fig. 2*U*). This was emulated by the mean of the top 15% of pixels showing a concentration peak in early G2 before being held at a stably high level through to mitosis (Fig. 2*X*). For Clp1, such an early cell cycle pattern of accumulation is not consistent with models for size sensing at the G2 to mitosis transition.

In the case of the G1- to S-phase proteins (Fig. 3), Cig2 (Fig. 3 *A* and *B*), Cdc18 (Fig. 3 *E* and *F*), Mik1 (Fig. 3 *G* and *H*), and Srw1 (Fig. 3 *I* and *J*) also showed whole-cell patterns of expression consistent with the imaging flow cytometry data (Fig. 1*G*). Being able to split septated cells from wide-field microscopy images meant that peak intensity for these proteins could be observed more clearly at the G1- to S-phase transition. For Cdc18 (Fig. 3*F*), Mik1 (Fig. 3*H*), and Srw1 (Fig. 3*J*), the highest concentrations were found in the shortest cells indicative of peak levels after binucleation and at the point of septation. For all three proteins, this level reduced to a low level by mid-G2. For Cdc10 as for imaging flow cytometry, the peak was only slightly elevated in short cells (∼1.2×) and was relatively stable through the rest of the cycle (Fig. 3 *K* and *L*). Cig2 concentration increased from G1 to a peak early in G2. Its level reduced as cells proceeded through the cell cycle to a low at mitosis (Fig. 3 *A* and *B*). The pattern of whole-cell Cig2 expression was matched by its nuclear concentration (Fig. 3*D*). We also report the visualization of endogenous Cig1 expression (Fig. 3*M*). While its expression level proved too low to accurately quantify by our methods of analysis, the images show visible Cig1-mNG fluorescence at both single and duplicated SPBs in G2 and then, transiently throughout the nucleus at anaphase and nuclear division (Fig. 3*M*). Overall, these results confirm our earlier conclusion that changes in cell cycle protein concentrations are more a feature of the G1- to S-phase transition than for G2 to mitosis.

Our nuclear screen suggested that five members of the core set of cell cycle CDK regulators Cdc2, Cdc13, Cdc25, Suc1, and Wee1 increase in nuclear concentration to a peak at mitotic entry. To confirm nuclear localization and quantify precise nuclear levels, we used a dual-color imaging approach to image each fluorescently tagged regulator alongside Cut11-mCherry, a component of the nuclear core complex, to mark the nucleus for segmentation. Fission yeast is particularly amenable to tracking of nuclear localization patterns throughout the whole-cell cycle due to having a closed mitosis. We used a combination of whole-cell neural network segmentation with YeaZ and machine learning nuclear segmentation with Ilastik (39) (*SI Appendix*, Fig. S2). Examining cells from asynchronous populations from early G2 through to septation allowed us to visually determine how the localization of these regulators changed (Fig. 4 and *SI Appendix*, Fig. S3). Taking Cdc2-mNG as an example (Fig. 4*A*), for cells in G2 the signal can be seen to be nuclear enriched (Fig. 3*A*) and to accumulate on the SPB, as previously observed (40). After SPB duplication, Cdc2 concentrates on both SPBs and the connecting spindle. As the nucleus elongates in anaphase, Cdc2 is exported from the nucleus prior to reaccumulation in the next cycle after nuclear division. In the associated dot plot (Fig. 4*B*), the mean cellular concentration for each cell (represented in blue) remains constant throughout the cell cycle, consistent with previous whole-cell measurements (Figs. 1*F* and 2*A*). Mononucleate nuclear Cdc2 concentration (green) increases with cell length throughout the cell cycle (Fig. 4*B*), reaching a peak at mitotic entry. In long mononucleates that are >12 μm, Cdc2 levels decrease again, thus indicating that Cdc2 leaves the nucleus in mitosis. Pink dots represent the nuclear concentration of binucleate cells that have not yet septated and show that nuclear levels of Cdc2 post-mitosis reduce to a level equal to the whole-cell concentration.

Nuclear concentration patterns for Cdc13 (Fig. 4*C*), Cdc25 (Fig. 4*D*), Suc1 (Fig. 4*E*), and Wee1 (Fig. 4*F*) match their "top 15%" analyses (Fig. 2 *H*, *L*, *P*, and *T*) and establish that these core CDK mitotic regulators all increase in concentration within the nucleus as cell size increases. For Cdc2, this appears to be a continuous increase correlated with size and more than

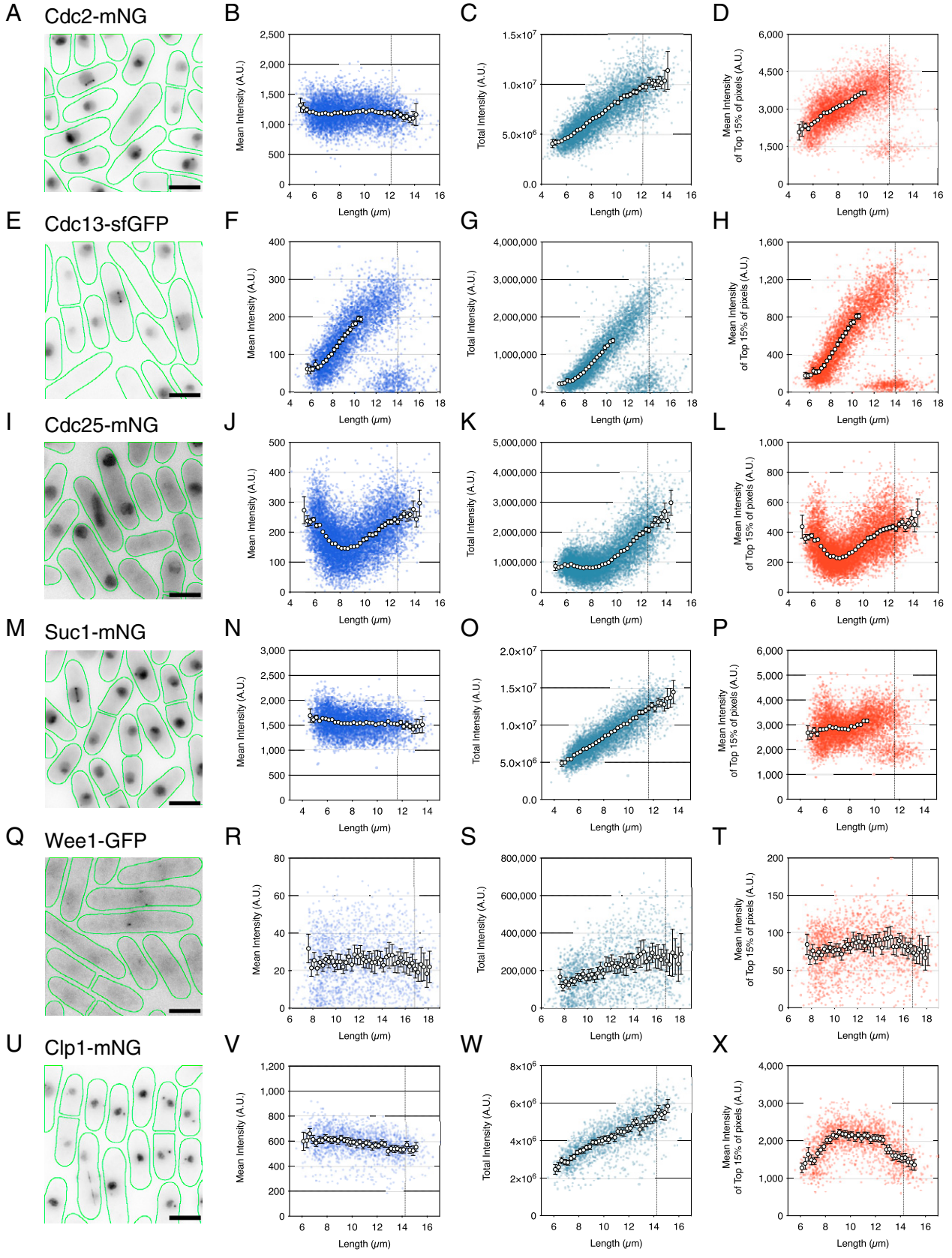

Fig. 2. The core mitotic regulators Cdc2, Cdc13, Cdc25, Suc1, and Wee1 increase their localized concentrations to a peak at mitotic entry, while Clp1 increases to a peak by early G2. (*A*, *E*, *I*, *M*, *Q*, and *U*) Images of fission yeast cells (green outlines) for Cdc2-mNG (*A*), Cdc13-sfGFP (*E*), Cdc25-mNG (*I*), Suc1-mNG (*M*), Wee1-GFP (*Q*), and Clp1-mNG (*U*) from asynchronous cell cultures, each showing a range of cells across the cell cycle. Images are maximum-intensity projections. (Scale bars: 5 μm.) (*B–D*, *F–H*, *J–L*, *N–P*, *R–T*, and *V–X*) The plots show mean whole-cell fluorescence intensity (blue), total cellular fluorescence intensity (teal), and mean of the top 15% of cellular pixel values (red) plotted as arbitrary units (A.U.) against cell length for Cdc2-mNG (*B–D*), Cdc13-sfGFP (*F–H*), Cdc25-mNG (*J–L*), Suc1-mNG (*N–P*), Wee1-GFP (*R–T*), and Clp1-mNG (*V–X*). Colored dots represent individual cell values. Circles represent the mean values at 0.25-μm-length bins with >10 cells/bin. Error bars represent 95% CIs. Means stop for *D*, *F–H*, and *P* before cell populations become bimodally distributed. Vertical dotted lines represent septation length. (*A–D*) n = 6,989 cells. (*E–H*) n = 5,895 cells. (*I–L*) n = 11,091 cells. (*M–P*) n = 6,513 cells. (*Q–T*) n = 1,863 cells. (*U–X*) n = 1,838 cells.

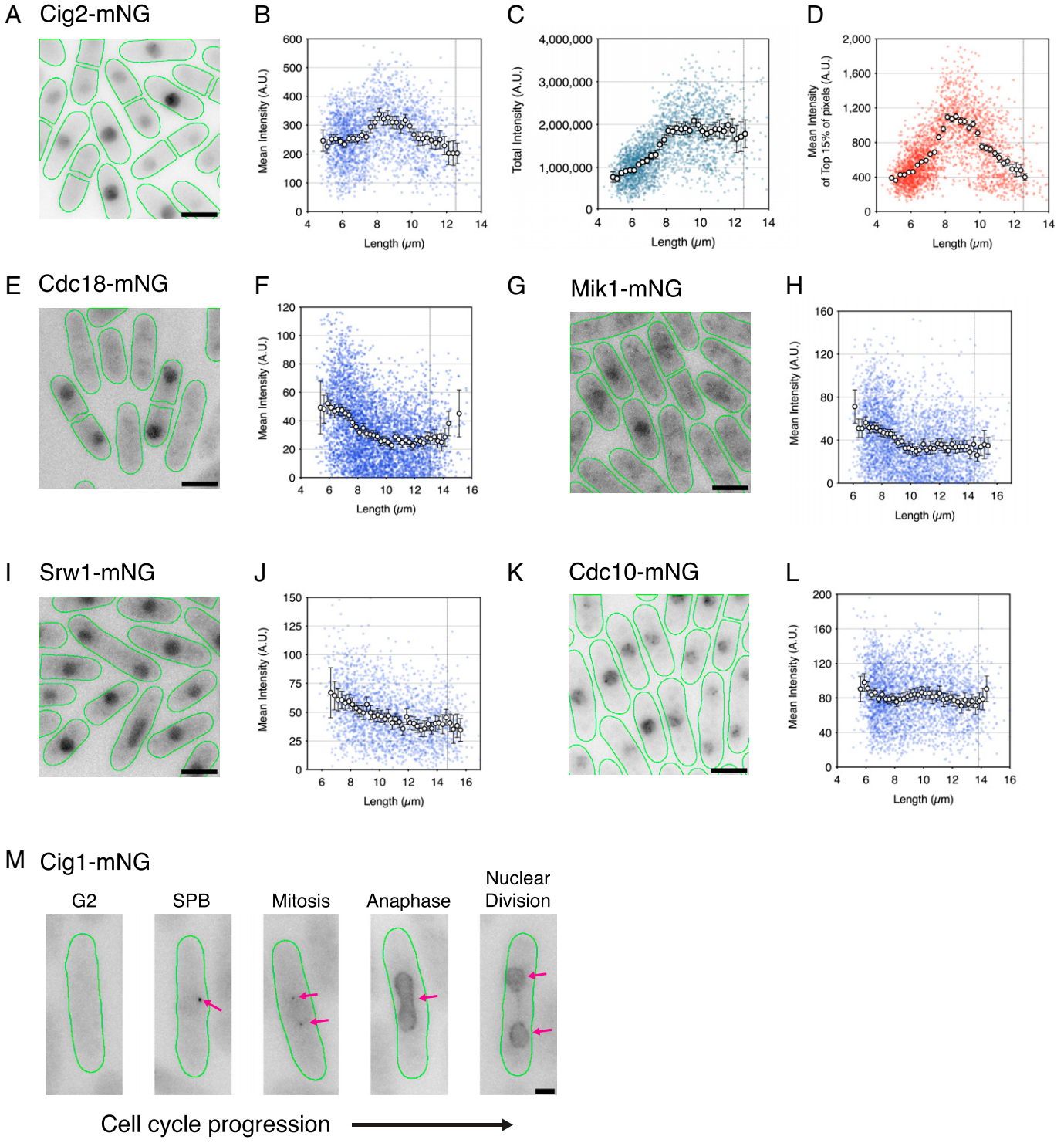

Fig. 3. G1- to S-phase transition proteins are transiently expressed early in the cell cycle. (*A*, *E*, *G*, *I*, and *K*) Images of fission yeast cells (green outlines) for Cig2-mNG (*A*), Cdc18-mNG (*E*), Mik1-mNG (*G*), Srw1-mNG (*I*), and Cdc10-mNG (*K*) from asynchronous cell cultures, each showing a range of cells across the cell cycle. Images are maximum-intensity projections. (Scale bars: 5 μm.) (*B*–*D*) Cig2-mNG plots show mean whole-cell fluorescence intensity (blue), total cellular fluorescence intensity (teal), and mean of the top 15% of cellular pixel values (red) plotted as arbitrary units (A.U.) against cell length. (*F*, *H*, *J*, and *L*) Mean whole-cell fluorescence intensity plots against cell length for Cdc18-mNG (*F*), Mik1-mNG (*H*), Srw1-mNG (*J*), and Cdc10-mNG (*L*). Colored dots represent individual cell values. Circles represent means at 0.25-μm-length bins with >10 cells per bin. Error bars represent 95% CIs. Vertical dotted lines represent septation length. (*B*–*D*) n = 2,953 cells. (*F*) n = 4,644 cells. (*H*) n = 3,683 cells. (*J*) n = 1,946 cells. (*L*) n = 2,978 cells. (*M*) Representative images of Cig1-mNG cells (green outlines) at progressive cell cycle stages. Images are maximum projections normalized to peak intensity levels (at SPB). Pink arrows indicate Cig1-mNG localization. (Scale bar: 2 μm.)

doubles in concentration from early G2 to mitosis (Fig. 4*B*). For Suc1, nuclear concentration increases at the beginning of the cell cycle, plateaus in mid-G2, and then, reaccumulates into mitosis, increasing 1.5× across the full cycle (Fig. 4*E*). Likewise, Wee1 nuclear concentration also increases 1.5×, with a continuous increase to mid-G2 followed by a plateau until mitosis (Fig. 4*F*). Unlike Cdc2, Cdc13, and Suc1, which show a rapid exit from the nucleus at mitotic exit as shown by

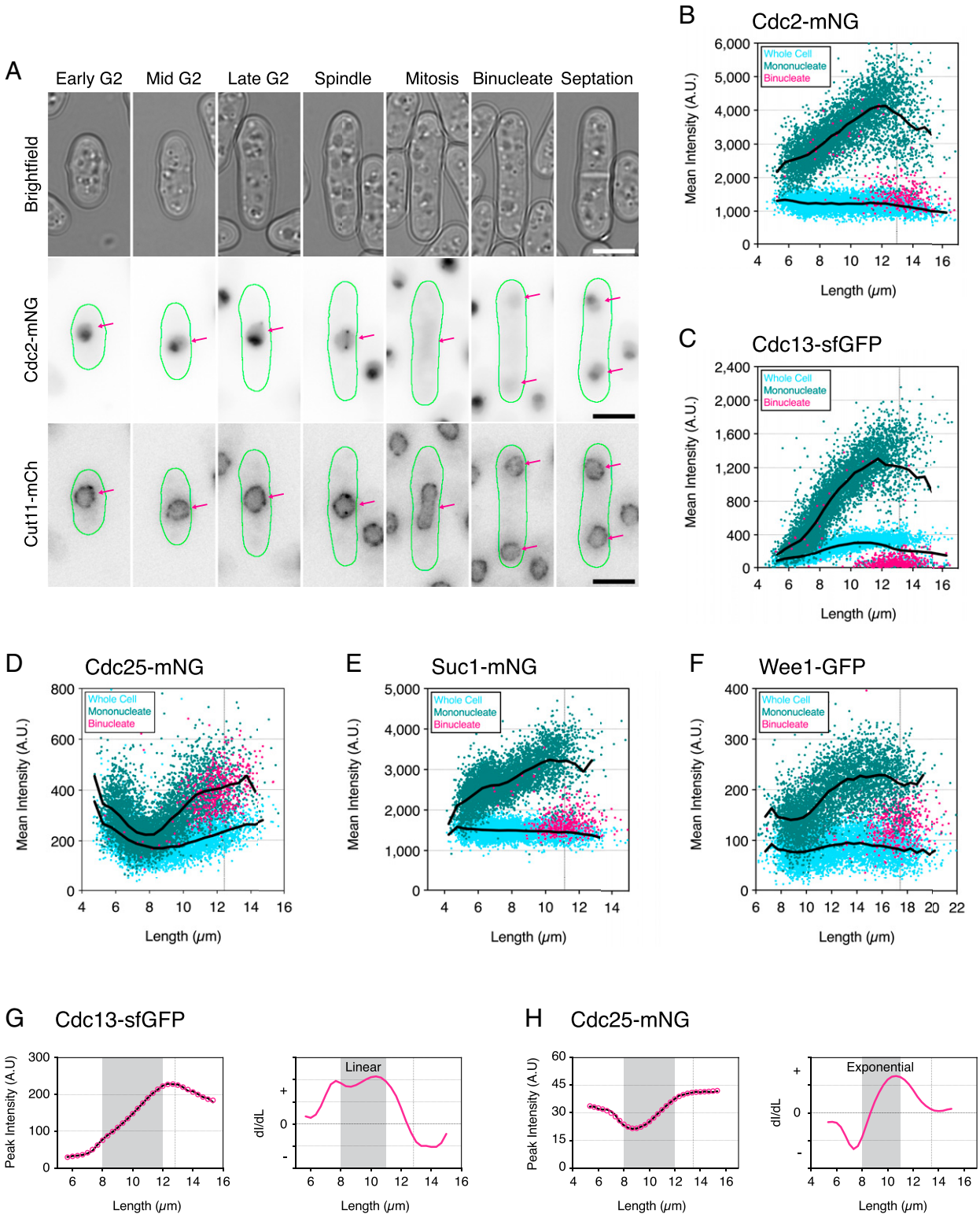

Fig. 4. The core mitotic regulators increase their nuclear concentrations to a peak in late G2. (*A*) Montage showing representative Cdc2-mNG cells (green outlines) selected from an asynchronous population at progressive stages of the fission yeast cell cycle from early G2 through to septation. (*Top*) Bright field. (*Middle*) Inverted fluorescence images for Cdc2-mNG. (*Bottom*) Inverted fluorescence images for Cut11-mCh (nuclear marker). mNG intensities are maximum-intensity projections normalized minimum to maximum for all pixels within the montage. Cut11-mCh images are maximum-intensity projections renormalized from 10,000- to 50,000-pixel values (64-bit images). Pink arrows indicate nuclei positions for comparison of Cdc2 localization. (Scale bars: 5 μm.) (*B*–*F*) Plots showing mean cellular fluorescence intensity (light blue), mean nuclear fluorescence for mononucleate cells (green), and binucleates (pink) as arbitrary units (A.U.) against cell length for Cdc2-mNG (*B*), Cdc13-sfGFP (*C*), Cdc25-mNG (*D*), Suc1-mNG (*E*), and Wee1-GFP (*F*). Colored dots represent individual cell values. Black lines represent connected mean values calculated at 0.5-μm bins for whole-cell values (lower lines) and nuclear mononucleate values (upper lines). Note that binucleates with a septum are split during segmentation, with each half treated as an individual mononucleate. Vertical dotted lines indicate septation length. (*B*) n = 5,857 cells. (*C*) n = 6,235 cells. (*D*) n = 5,920 cells. (*E*) n = 5,832 cells. (*F*) n = 5,189 cells. (*G* and *H*) Rate of change plots for nuclear accumulation of Cdc13-sfGFP (*F*) and Cdc25-mNG (*G*). For each strain, plots in *Left* show mean peak nuclear intensity (peak intensity) against cell length. Raw data values are in black, and smoothed data values are in pink. Plots in *Right* are the rate of change of intensity of smoothed data (derivative Intensity (dI)/derivative Length (dL))/cell length (μm) from each unit of length to the next. Positive values indicate accumulation, while negative points indicate loss. Increasing values indicate an increasing rate of accumulation. Values at zero indicate a stable concentration. Vertical dotted lines on the plots indicate cell length at mitosis. (G) n = 194,326 cells. (*H*) n = 223,364 cells.

nucleus levels of binucleate cells matching the level of the whole cell, Wee1 appears to be only partially exported as indicated by binucleate nuclear levels being raised above the level of the whole cell. For Cdc25 in Fig. 2*J*, we showed that whole-cell levels increased nearly twofold from mid-G2 to mitosis, and this is recapitulated in Fig. 4*D*. Nuclear accumulation of Cdc25 follows a similar pattern but at a higher concentration than compared with whole-cell levels, with nuclear levels again increasing around twofold from mid-G2 to mitosis and then, maintained at a high level after binucleation. Cdc25 nuclear export begins at the point of septation, with faint puncta observed at the nuclear periphery suggestive of active nuclear export (*SI Appendix*, Fig. S3*B*). Nuclear levels gradually decrease in concentration in early G2 (in short cells <8 μm).

The protein that changed most significantly was the mitotic B-type cyclin Cdc13. In the whole cell, the change in concentration is ∼4 to 5× (Figs. 2*F* and 4*C*), which is amplified in the nucleus to 8 to 10× (Fig. 4*C*). This change is concentration is higher than the twofold change in concentration observed in our imaging flow cytometry analysis (Fig. 1 *D* and *F*), where Cdc13 levels were averaged by binned length and included bimodal populations at long lengths, which reduce the average. This high dynamic range through the cell cycle, particularly in the nucleus, makes Cdc13 the best for a candidate cell size sensor.

Returning to our imaging flow cytometry data, we looked to measure the nuclear rate of change for Cdc13 and Cdc25. From mid-G2 toward mitotic entry (8 to 12 μm), we find that nuclear accumulation of Cdc13 occurs at an almost constant linear rate after a rise at the beginning and a fall at the end of the cell cycle (Fig. 4*G*). In contrast, the rate of Cdc25 nuclear accumulation increases in an exponential manner during the second half of the cell cycle (Fig. 4*H*). Cdc13 and Cdc25 both activate the G2–M CDK but in different ways; Cdc13 forms a complex with Cdc2 for direct activation, while Cdc25 phosphatase activates by removing the inhibitory Cdc2-Y15 phosphorylation. This suggests that the mode of CDK regulation during the cell cycle switches from a mode that is predominantly dependent upon cyclin accumulation to a mode that is additionally subject to the futile cycle of the activating Cdc25 phosphatase counteracting the inhibitory action of Wee1 protein kinase.

Discussion

In this paper, we have determined how the levels of potential mitotic regulators change during the cell cycle in both the whole cell and the nucleus of fission yeast, with the aim of informing our understanding of how cells sense their size and regulate the dynamics of CDK activation at the onset of mitosis. We measured the levels of 30 proteins previously identified as potential mitotic regulators (23, 24) throughout the cell cycle together with 8 more proteins implicated in mitotic control and a further 7 involved in the G1- to S-phase transition. Surprisingly, of the 38 G2 to mitosis regulators, 36 remained constant in concentration within the whole cell throughout the cell cycle. Therefore, if they were to have an influence on cell cycle progression through CDK regulation, this would have to be due to dynamic changes in their activity status: for example, by changing phosphorylation levels or through changes in their spatial distribution. Only two mitotic regulators, the mitotic B-type cyclin Cdc13 and the activating Cdc25 phosphatase, change in whole-cell levels, with both peaking at the onset of mitosis.

The behavior of the seven proteins involved in the G1- to S-phase transition was different, with four changing dynamically in the whole cell during the cell cycle, peaking at G1–S. We propose that changes in the level of protein concentration are more a feature at the G1- to S-phase transition than G2 to mitosis. Three of the four proteins (Cdc18, Mik1, and Cig2) are encoded by genes that are regulated by Cdc10 and are transcriptionally induced at the G1- to S-phase transition. We think it is unlikely that these four proteins are involved in cell size sensing at the G1- to S-phase transition because although there is a cell size checkpoint at this stage of the cell cycle in fission yeast, it is cryptic in wild type–sized cells and does not normally influence cell size at S phase or at mitosis and cell division (41, 42). Periodic transcription leading to S-phase regulators attaining a critical concentration may be a feature of the G1- to S-phase transition, reflecting a control that is time dependent rather than cell size dependent. In budding yeast, it has been suggested that S-phase regulators need to attain a concentration before S phase can commence, but in these cases, the control has been related to cell size sensing (12, 43, 44).

Over three-quarters of the cell cycle proteins investigated were primarily located in the nucleus during interphase, and 29 of them accumulated in the nucleus to a higher level than the cytoplasm. This nuclear enrichment could be due to critical cell cycle events occurring in the nucleus. Seven proteins were also associated with the SPB, including core CDK regulators (Cdc2, Cdc13, Clp1, Suc1, Wee1, Cig1, Cig2, and Cdr2), providing support for the long-held view that the centrosome plays a critical role in cell cycle control (45, 46). Nine of the 29 nuclear-located proteins undergo significant changes during the cell cycle, 6 of which are core CDK regulators (Cdc2, Cdc13, Cdc25, Suc1, Wee1, and Cig2). This finding supports work from mammalian systems that cell cycle–regulated nuclear import plays an important role in allowing the cell to reach the point of mitotic onset by gradually bringing about the nuclear accumulation of mitotic CDK regulators (47). Consistent with nuclear transport playing a regulatory role is the fact that 6 of the 17 genes identified in the haploinsufficient screen are involved in nuclear transport (23). One of the nuclear-located proteins, such as Cdc13, increases to a greater extent in the nucleus than is the case for the cytoplasm. These various observations suggest that nuclear localization of cell cycle regulators plays a significant role in cell cycle control and that nuclear transport plays a key role in this process.

The fact that many of the cell cycle proteins and DNA are nuclear localized has implications for ploidy-sensing mechanisms. Relevant to this is the observation that in certain mutant fission yeast strains, haploid and diploid cells have equal levels of Cdc13 but lower levels of CDK protein kinase activity (8). The other nuclear-located core CDK regulators identified in this study may be relevant for this phenomenon as well. It will be important in future work to determine how their levels behave in cells of different ploidy and in haploinsufficient strains, including those involved in nuclear transport (23).

The control of CDK activity required for mitotic onset is highly dependent upon both the level of the Cdc2 activating mitotic B-type cyclin Cdc13 and the regulatory feedback loop consisting of the counteracting phosphatase activator Cdc25 and the protein kinase inhibitor Wee1 (27, 48). This regulatory loop determines the extent of the inhibitory Cdc2 Y15 phosphorylation. We have shown that the whole-cell concentration of Wee1 remains reasonably constant, but Cdc25 levels oscillate significantly through the cell cycle. This suggests that the activating potential of the Cdc25/Wee1 regulatory loop follows the Cdc25 concentration profile by being high at the beginning of

the cell cycle at a time when cyclin–CDK nuclear levels are low, falling to a low by mid-G2, and then, rising toward mitosis onset. When Wee1 is inactivated by a temperature shift of a $Wee1^{ts}$ mutant, cells in the second half of G2 are immediately advanced into mitosis (26). This indicates that the Cdc25/Wee1 regulatory loop is restraining mitotic onset during the second half of G2, even though there is sufficient CDK formed by the Cdc13/Cdc2 complex in mid-G2 for mitotic onset to take place.

Cdc13 concentration rises dramatically throughout the cell cycle, much more than any other protein investigated in this study. This level rises 4 to 5× in the whole cell and 8 to 10× in the nucleus. Low Cdc13 levels at the beginning of the cycle correspond with low nuclear levels of Cdc2 and the CDK regulatory unit Suc1, suggesting that Cdc13 levels may be limiting for their nuclear import and therefore, acting as a break for high nuclear CDK levels early in the cycle. At the point in mid-G2 when the Cdc25/Wee1 regulatory loop begins to rise, Cdc13 concentration is about two-thirds of the maximum reached at the onset of mitosis. We conclude that this level of cyclin is sufficient to generate enough CDK activity to undergo mitosis but is restrained by the Cdc25/Wee1 regulatory loop until late in G2. The difference in Cdc13 concentration from mid-G2 to mitotic onset is about one-third, which could correspond to a "CDK buffer zone," where cells undergo mitosis with a higher level of CDK activity than is strictly necessary for the completion of mitosis (17, 49).

We propose that the increasing level of Cdc13 is primarily responsible for cell size sensing at the G2 to mitosis transition (17) and that this is the major mechanism by which eukaryotic cells maintain cell size homeostasis at cell division. As B-type cyclin increases in concentration throughout the cell cycle and peaks at mitosis in all eukaryotes investigated thus far, this could be a universal cell size–sensing mechanism, with the advantage over cell geometry–sensing mechanisms (13–16) of being independent of a fixed cell shape and therefore, having the potential to be applicable to all cell types, including metazoans.

The observations we have reported here also have implications for the dynamics of CDK regulation at the onset of mitosis. We have proposed that the increasing level of the B-type cyclin Cdc13 is primarily responsible for cell size sensing at the G2 to mitosis transition, with a possible further contribution provided by the increasing level of Cdc25 during the latter part of G2 (33). Our analysis suggests that the minimum level of Cdc13 required for mitosis and cell division is established in mid-G2 when the cell attains a threshold size. However, the linear increase in Cdc13 level from mid-G2 to mitosis likely results in a change in CDK activity, which is too gradual at the end of the cell cycle to bring about an orderly sharp transition into mitosis. We propose that the cell solves this problem by a two-step process. The first step is based on B-type cyclin Cdc13 accumulation that can accurately monitor cell size while Cdc25 levels are reducing and low. The second step, activated in mid-G2, is based upon the Cdc25/Wee1 regulatory loop. The increasing Cdc25 level sets up a futile cycle introducing bistability, which results in a rapid rise in CDK activity and a sharp orderly progression through the multiple events of mitosis, thereby reducing the variability in size at division. Accumulation in the nucleus in a size-dependent manner could also amplify any potential cell size–sensing mechanism (47, 50).

This study has shown that the only candidates among the 38 we investigated for cell cycle regulators that could increase with cell size are Cdc13 and Cdc25. The concentration of Cdc13 increases linearly throughout the cell cycle as cell size increases, but that is not the case for Cdc25, the concentration of which decreases as cell size increases during the first half of the cell cycle and only increases from a point in G2. Therefore, changes in the level of Cdc25 mean that it is likely to only make a minor contribution to cell size sensing. However, to establish that the Cdc13 level does act as a cell size sensor requires further experiments that alter the level of Cdc13 and relate those changes to the effects they may have on cell size at mitosis and cell division. Preliminary experiments have been carried out that show large changes in Cdc13 expression levels can influence cell size at division (17), but there is a need for more detailed studies involving smaller alterations in Cdc13 level to strengthen the case that is a cell size sensor.

It is striking, however, that in all eukaryotes studied so far, mitotic B-type cyclin rises in level throughout the cell cycle, so it would be a good candidate as a universal cell size sensor. In addition, a Cdc25-like phosphatase and a Wee1 protein kinase regulating CDK activity control of tyrosine phosphorylation of the CDK protein kinase (51–53) have been widely observed throughout eukaryotic cells. Therefore, this two-step model of mitotic B-type cyclin accumulation through the cell cycle–sensing cell size, coupled with a subsequent Cdc25/Wee1 futile cycle introducing bistability and rapid CDK activation, may be a universal feature of eukaryotic cell cycle control given the conservation of the control elements throughout eukaryotes.

Materials and Methods

Lead Contact and Materials Availability. Further information and requests for resources and reagents should be directed to P.N.

All strains, plasmids, and reagents generated in this study are available without restriction.

***S. pombe* Culture.** Cells were cultured by standard growth methods as previously described (51) first on solid YE4S agar and then, in liquid Edinburgh minimal media supplemented with 20.0 g/L dextrose anhydrous (BP350-1; Fisher Scientific) and 5.0 g/L ammonium chloride (A9434; Sigma; supplemented with adenine, leucine, histidine, and uracil to a concentration of 0.15 g/L for autotrophic markers if required) added postautoclaving and filtered (0.22 μm). Cells were grown at 25 °C and maintained in exponential growth between 2×10^6 and 1×10^7 cells/mL (ideally imaged at $\sim 5 \times 10^6$ cells/mL).

Strains. *SI Appendix*, Table S1 has a complete list and full genotypes of *S. pombe* strains used in this study. Strains generated specifically for this study were constructed using standard methods (51, 52). C-terminal gene tagging was performed as previously described (53) using standard primers (listed in *SI Appendix*, Table S2) designed from the Bähler laboratory web interface (bahlerlab.info/resources/) for pFA6a vector templates carrying kanamycin or GFP-hygromycin resistance cassettes using the lithium acetate method of transformation. pFA6a-Kan vectors were modified by James Patterson for mNeonGreen tagging to incorporate a nonstandard linker (GATTCTGCTGGA TCAGCTGGC) upstream of mNeonGreen to replace the standard forward linker (CGGATCCCCGGGTTAATTAA).

Fluorescence Microscopy. For wide-field microscopy, 1.5 mL of 0.4 to 0.5 OD^{595} culture was centrifuged at 3,000 rpm for 30 s, with the supernatant removed, and the process was repeated; 1.75 μL of pelleted cells were plated on a microscope slide, spread, and flattened with the addition of a coverslip. Live cells were imaged within 10 min of preparation. All microscopy was performed at 25 °C using a Nikon Ti2 Inverted microscope with a 100× Plan Apochromat oil immersion objective (NA 1.45), the Perfect Focus System, a Prime sCMOS camera (Photometrics), and an Okolab environmental chamber. The microscope was controlled with Micro-Manager version 2.0 software (54). Fluorescence excitation was performed with a SpectraX LED light engine (Lumercor) fitted with standard filters: 470/24 for imaging mNG/sfGFP/GFP and 575/25 for mCherry with a dual-edge Chroma 59022bs, ET-EGFP/mCherry dichroic beam splitter. Emission filters used were Chroma ET-EGFP single-band bandpass filter (ET525_50m) for mNG/sfGFP/GFP and Semrock 641-/75-nm bright-line single-band bandpass filter (FF02_641_75) for mCherry.

Wide-Field Image Processing. Basic image processing was carried out with FIJI software (55). Whole-cell segmentation was performed using the convolutional neural network YeaZ (34) trained for fission yeast segmentation on bright-field image slices 1 μm below the focal plane. Using FIJI, maximum-intensity projections were made of sfGFP/GFP/mNG/mCherry images covering 2 μm around the focal plane. The machine learning tool Ilastik (39) was trained and used to segment maximum projection mCherry images to create nuclear masks. For background correction, controls without the fluorescent tag of interest for each experiment were imaged to give a measure of mean autofluorescence. This value was subtracted from whole-cell and nuclear concentration measurements.

Imaging Flow Cytometry and Postprocessing. Cells were imaged for bright field and fluorescence (488 laser at 400 mW) with an Amnis Imagestream X Mk II Imaging Flow Cytometer with a 60× objective lens. Cells were concentrated from asynchronous exponentially growing cultures ($OD^{595} \sim 0.4$ to 0.5) by centrifugation (3,000 rpm/30 s), resuspended in >50 μL of media, and water bath sonicated for 15 s. Prior to acquisition, cells were gated based upon BF gradient RMS values (value of cell focus) of 65 to 78 and area/aspect ratio values consistent with single cells. Approximately 250,000 gated cells were acquired in 10- to 15-min experiments, with an acquisition rate of 300 to 500 gated cells/s.

Postacquisition processing was undertaken with Amnis IDEAS 6.2 data exploration and analysis software. Cell segmentation masks were created from BF images: Erode(MO1, 3) named Pombe_Mask and overlaid onto fluorescent images (Ch02).

Cells were further gated based on

R1: Width_Pombe X coordinates: 3.75 to 6.75;
R2: Thickness_Max_Pombe of R1 X coordinates: 3.75 to 6.75;
R3: Thickness_Min_Pombe of R2 X coordinates: 3.1 to 5.5;
R4: Gradient_RMS_MO1_Ch01 of R3 X coordinates: 65 to 78; and
R5: Intensity_Pombe_Ch02: removal of extremes on a strain-by-strain basis.

Background correction was based upon imaging of a nonfluorescent control on each experimental day. Mean autofluorescence per length bin was calculated as a linear regression and used to calculate the level of background to be subtracted from total, mean, and maximum pixel fluorescent values.

Derivative Analyses. To calculate the d(intensity)/d(length) values at the required lengths, we first calculated the density of the experimentally measured points in the two-dimensional intensity vs. length space. We used the kde2d MATLAB routine, which uses a second-order Gaussian kernel with an automatic bandwidth selection method (56). The peak density at each length is then determined to give the intensity value, which is then differentiated with respect to length.

Calculation of the Number of Nuclei and Nuclear Intensity. Using a previous approach (8, 17), we extracted the individual cell tiff images for the bright field and each fluorescence channel from the .cif file generated by the ImageStream X instrument. A cell mask is generated from the bright-field image using a simple grayscale Otsu threshold for this image. The medial line for the cell mask is defined, and the nuclear marker fluorescence intensity is measured at each point along this line. A simple peak detection algorithm is used to detect if the cell is mono- or binucleated. The fluorescence intensity level for each nucleus is simply determined by measuring the pixel value from the fluorescence intensity at this position along the medial line.

Graphs and Statistics. A custom MATLAB script was used for whole-cell, nuclear, and top percentage background-subtracted fluorescence measurements for wide-field imaging (script author: G.D.). This script counted the number of nuclei per cell, with cells having more than two nuclear objects considered binucleate (Ilastik segmentation often found pieces of nuclear bridge). All plots and statistical analyses were performed with GraphPad Prism 9 except for heat maps (Fig. 1), which were produced by a custom MATLAB script of background-subtracted whole-cell mean data collected from imaging flow cytometry. Statistical analyses used and *n* numbers are stated in the figures.

Data, Materials, and Software Availability. Processed data used for the plots in the main figures have been deposited to GitHub (https://github.com/scottcurran10/fission-yeast-cell-cycle/SOURCE_DATA_CurranS_PNAS_2022) (57). Widefield microscopy images, Imagestream files (including .cif, .rif & .daf files) and raw data are available upon request to P.N.

Scripts and code have been deposited in GitHub (https://github.com/scottcurran10/fission-yeast-cell-cycle) (58). The use of this code is governed by a Massachusetts Institute of Technology license. Extended supplemental data have been deposited in Figshare (https://figshare.com/articles/dataset/ExtendedSI_PNAS_Curran_2022_pdf/20362389/2) (35).

ACKNOWLEDGMENTS. We thank the laboratories of Silke Hauf and Yasushi Hiraoka for sharing of *S. pombe* strains; Sahand Jamal Rahi for training of YeaZ for fission yeast cell segmentation; James Patterson (previous member of the laboratory of P.N.) for construction and sharing of plasmids; and members of the laboratory of P.N. Thomas Hammond, Emma Roberts, and Theresa Zeisner and previous member Tiffany Mak for critical reading of the manuscript and comments. S.C. and P.N. were supported by the Francis Crick Institute, which receives its core funding from Cancer Research UK Grant FC01121, UK Medical Research Council Grant FC01121, and Wellcome Trust Grant FC01121. In addition, this work was supported by Wellcome Trust Grants 214183 (to P.N.) and 093917 (to P.N.). G.D. acknowledges University College London, Wellcome Trust Grant 203276/Z/16/Z, and the European Molecular Biology Laboratory for support. P.R. acknowledges the support of Biotechnology and Biological Sciences Research Council Grant BB/P026818/1 and Engineering and Physical Science Research Council Grant EP/N013506/1.

1. J. M. Mitchison, Growth during the cell cycle. *Int. Rev. Cytol.* **226**, 165–258 (2003).
2. M. B. Ginzberg, R. Kafri, M. Kirschner, On being the right (cell) size. *Science* **348**, 1245075 (2015).
3. A. C. Lloyd, The regulation of cell size. *Cell* **154**, 1194–1205 (2013).
4. P. A. Fantes, Control of cell size and cycle time in *Schizosaccharomyces pombe*. *J. Cell Sci.* **24**, 51–67 (1977).
5. E. Wood, P. Nurse, Pom1 and cell size homeostasis in fission yeast. *Cell Cycle* **12**, 3228–3236 (2013).
6. E. Wood, P. Nurse, Sizing up to divide: Mitotic cell-size control in fission yeast. *Annu. Rev. Cell Dev. Biol.* **31**, 11–29 (2015).
7. D. O. Robinson *et al.*, Ploidy and size at multiple scales in the *Arabidopsis* Sepal. *Plant Cell* **30**, 2308–2329 (2018).
8. J. O. Patterson, S. Basu, P. Rees, P. Nurse, CDK control pathways integrate cell size and ploidy information to control cell division. *eLife* **10**, e64592 (2021).
9. P. Jorgensen *et al.*, The size of the nucleus increases as yeast cells grow. *Mol. Biol. Cell* **18**, 3523–3532 (2007).
10. M. G. Lee, P. Nurse, Complementation used to clone a human homologue of the fission yeast cell cycle control gene cdc2. *Nature* **327**, 31–35 (1987).
11. D. Keifenheim *et al.*, Size-dependent expression of the mitotic activator Cdc25 suggests a mechanism of size control in fission yeast. *Curr. Biol.* **27**, 1491–1497.e4 (2017).
12. K. M. Schmoller, J. J. Turner, M. Kõivomägi, J. M. Skotheim, Dilution of the cell cycle inhibitor Whi5 controls budding-yeast cell size. *Nature* **526**, 268–272 (2015).
13. J. B. Moseley, A. Mayeux, A. Paoletti, P. Nurse, A spatial gradient coordinates cell size and mitotic entry in fission yeast. *Nature* **459**, 857–860 (2009).
14. S. G. Martin, M. Berthelot-Grosjean, Polar gradients of the DYRK-family kinase Pom1 couple cell length with the cell cycle. *Nature* **459**, 852–856 (2009).
15. K. Z. Pan, T. E. Saunders, I. Flor-Parra, M. Howard, F. Chang, Cortical regulation of cell size by a sizer cdr2p. *eLife* **3**, e02040 (2014).
16. G. Facchetti, B. Knapp, I. Flor-Parra, F. Chang, M. Howard, Reprogramming Cdr2-dependent geometry-based cell size control in fission yeast. *Curr. Biol.* **29**, 350–358.e4 (2019).
17. J. O. Patterson, P. Rees, P. Nurse, Noisy cell-size-correlated expression of cyclin B drives probabilistic cell-size homeostasis in fission yeast. *Curr. Biol.* **29**, 1379–1386.e4 (2019).
18. N. Rhind, Cell size control via an unstable accumulating activator and the phenomenon of excess mitotic delay *Bioessays*, 10.1002/bies.201700184 (2017).
19. M. D'Ario *et al.*, Cell size controlled in plants using DNA content as an internal scale. *Science* **372**, 1176–1181 (2021).
20. D. O. Morgan, Cyclin-dependent kinases: Engines, clocks, and microprocessors. *Annu. Rev. Cell Dev. Biol.* **13**, 261–291 (1997).
21. D. U. Kim *et al.*, Analysis of a genome-wide set of gene deletions in the fission yeast *Schizosaccharomyces pombe*. *Nat. Biotechnol.* **28**, 617–623 (2010).
22. J. Hayles *et al.*, A genome-wide resource of cell cycle and cell shape genes of fission yeast. *Open Biol.* **3**, 130053 (2013).
23. N. Moris *et al.*, A genome-wide screen to identify genes controlling the rate of entry into mitosis in fission yeast. *Cell Cycle* **15**, 3121–3130 (2016).
24. F. J. Navarro, P. Nurse, A systematic screen reveals new elements acting at the G2/M cell cycle control. *Genome Biol.* **13**, R36 (2012).
25. P. Russell, P. Nurse, cdc25+ functions as an inducer in the mitotic control of fission yeast. *Cell* **45**, 145–153 (1986).
26. P. Nurse, Genetic control of cell size at cell division in yeast. *Nature* **256**, 547–551 (1975).
27. K. L. Gould, P. Nurse, Tyrosine phosphorylation of the fission yeast cdc2+ protein kinase regulates entry into mitosis. *Nature* **342**, 39–45 (1989).
28. P. Russell, P. Nurse, Negative regulation of mitosis by wee1+, a gene encoding a protein kinase homolog. *Cell* **49**, 559–567 (1987).

29. J. M. Mitchison, P. Nurse, Growth in cell length in the fission yeast *Schizosaccharomyces pombe*. *J. Cell Sci.* **75**, 357–376 (1985).
30. N. C. Shaner *et al.*, A bright monomeric green fluorescent protein derived from Branchiostoma lanceolatum. *Nat. Methods* **10**, 407–409 (2013).
31. H. Masuda, C. S. Fong, C. Ohtsuki, T. Haraguchi, Y. Hiraoka, Spatiotemporal regulations of Wee1 at the G2/M transition. *Mol. Biol. Cell* **22**, 555–569 (2011).
32. J. Kamenz, T. Mihaljev, A. Kubis, S. Legewie, S. Hauf, Robust ordering of anaphase events by adaptive thresholds and competing degradation pathways. *Mol. Cell* **60**, 446–459 (2015).
33. S. Moreno, P. Nurse, P. Russell, Regulation of mitosis by cyclic accumulation of p80cdc25 mitotic inducer in fission yeast. *Nature* **344**, 549–552 (1990).
34. N. Dietler *et al.*, A convolutional neural network segments yeast microscopy images with high accuracy. *Nat. Commun.* **11**, 5723 (2020).
35. S. Curran, P. Nurse, G. Dey, P. Rees, Extended Supplementary Information for 'A quantitative and spatial analysis of cell cycle regulators during the fission yeast cell cycle', Curran et al., 2022. Figshare. https://figshare.com/articles/dataset/ExtendedSI_PNAS_Curran_2022_pdf/20362389/2. Deposited 22 July 2022.
36. F. R. Neumann, P. Nurse, Nuclear size control in fission yeast. *J. Cell Biol.* **179**, 593–600 (2007).
37. H. Cantwell, P. Nurse, A systematic genetic screen identifies essential factors involved in nuclear size control. *PLoS Genet.* **15**, e1007929 (2019).
38. H. Cantwell, P. Nurse, Unravelling nuclear size control. *Curr. Genet.* **65**, 1281–1285 (2019).
39. S. Berg *et al.*, Ilastik: Interactive machine learning for (bio)image analysis. *Nat. Methods* **16**, 1226–1232 (2019).
40. A. Decottignies, P. Zarzov, P. Nurse, In vivo localisation of fission yeast cyclin-dependent kinase cdc2p and cyclin B cdc13p during mitosis and meiosis. *J. Cell Sci.* **114**, 2627–2640 (2001).
41. P. Fantes, P. Nurse, Control of cell size at division in fission yeast by a growth-modulated size control over nuclear division. *Exp. Cell Res.* **107**, 377–386 (1977).
42. P. Nurse, P. Thuriaux, Controls over the timing of DNA replication during the cell cycle of fission yeast. *Exp. Cell Res.* **107**, 365–375 (1977).
43. S. Dorsey *et al.*, G1/S transcription factor copy number is a growth-dependent determinant of cell cycle commitment in yeast. *Cell Syst.* **6**, 539–554.e11 (2018).
44. F. S. Heldt, R. Lunstone, J. J. Tyson, B. Novák, Dilution and titration of cell-cycle regulators may control cell size in budding yeast. *PLOS Comput. Biol.* **14**, e1006548 (2018).
45. I. M. Hagan, A. Grallert, Spatial control of mitotic commitment in fission yeast. *Biochem. Soc. Trans.* **41**, 1766–1771 (2013).
46. M. Jackman, C. Lindon, E. A. Niggt, J. Pines, Active cyclin B1–Cdk1 first appears on centrosomes in prophase. *Nat. Cell Biol.* **5**, 143–148 (2003).
47. S. D. M. Santos, R. Wollman, T. Meyer, J. E. Ferrell Jr., Spatial positive feedback at the onset of mitosis. *Cell* **149**, 1500–1513 (2012).
48. R. Aligue, L. Wu, P. Russell, Regulation of *Schizosaccharomyces pombe* Wee1 tyrosine kinase. *J. Biol. Chem.* **272**, 13320–13325 (1997).
49. S. Basu, J. Greenwood, A. W. Jones, P. Nurse, Core control principles of the eukaryotic cell cycle. *Nature* **607**, 381–386 (2022).
50. A. R. Araujo, L. Gelens, R. S. Sheriff, S. D. Santos, Positive feedback keeps duration of mitosis temporally insulated from upstream cell-cycle events. *Mol. Cell* **64**, 362–375 (2016).
51. S. Moreno, A. Klar, P. Nurse, Molecular genetic analysis of fission yeast *Schizosaccharomyces pombe*. *Methods Enzymol.* **194**, 795–823 (1991).
52. S. L. Forsburg, N. Rhind, Basic methods for fission yeast. *Yeast* **23**, 173–183 (2006).
53. J. Bähler *et al.*, Heterologous modules for efficient and versatile PCR-based gene targeting in *Schizosaccharomyces pombe*. *Yeast* **14**, 943–951 (1998).
54. A. D. Edelstein *et al.*, Advanced methods of microscope control using μManager software. *J. Biol. Methods* **1**, e10 (2014).
55. J. Schindelin *et al.*, Fiji: An open-source platform for biological-image analysis. *Nat. Methods* **9**, 676–682 (2012).
56. Z. Botev, Kernal density estimation, version 1.3.0.0. https://www.mathworks.com/matlabcentral/fileexchange/17204-kernal-density-estimation. Accessed 1 March 2022.
57. S. Curran, Fission-yeast-cell-cycle. GitHub. https://github.com/scottcurran10/fission-yeast-cell-cycle/tree/main/SOURCE%20DATA_CurranS_PNAS_2022. Deposited 18 August 2022.
58. S. Curran, Fission-yeast-cell-cycle. GitHub. https://github.com/scottcurran10/fission-yeast-cell-cycle. Deposited 18 August 2022.